

Magnetic States and Electronic Properties of Manganese-Based Intermetallic Compounds Mn_2YZ and Mn_3Z ($Y = V, Cr, Fe, Co, Ni$; $Z = Al, Ge, Sn, Si, Pt$)

Vyacheslav V. Marchenkov * and Valentin Yu. Irkhin

M.N. Mikheev Institute of Metal Physics, UB RAS, 620108 Ekaterinburg, Russia;

*Correspondence: march@imp.uran.ru; valentin.irkhin@imp.uran.ru

Abstract: We present a brief review of experimental and theoretical papers on studies of electron transport and magnetic properties in manganese-based compounds Mn_2YZ and Mn_3Z ($Y = V, Cr, Fe, Co, Ni$, etc.; $Z = Al, Ge, Sn, Si, Pt$, etc.). It has been shown that in the electronic subsystem of Mn_2YZ compounds, the states of a half-metallic ferromagnet and a spin gapless semiconductor can arise with the realization of various magnetic states, such as a ferromagnet, a compensated ferrimagnet, and a frustrated antiferromagnet. Binary compounds of Mn_3Z have the properties of a half-metallic ferromagnet and a topological semimetal with a large anomalous Hall effect, spin Hall effect, spin Nernst effect, and thermal Hall effect. Their magnetic states are also very diverse: from a ferrimagnet and an antiferromagnet to a compensated ferrimagnet and a frustrated antiferromagnet, as well as an antiferromagnet with a kagome-type lattice. It has been demonstrated that the electronic and magnetic properties of such materials are very sensitive to external influences (temperature, magnetic field, external pressure), as well as the processing method (cast, rapidly quenched, nanostructured, etc.). Knowledge of the regularities in the behavior of the electronic and magnetic characteristics of Mn_2YZ and Mn_3Z compounds can be used for applications in micro- and nanoelectronics and spintronics.

Keywords: manganese based intermetallic compounds; antiferromagnetism; compensated ferrimagnetism; frustrated magnets; half-metallic ferromagnets; spin gapless semiconductors; topological semimetals; anomalous Hall effect; kagome lattice

1. Introduction

The exploration and advancement of novel materials with distinct magnetic and electronic properties, along with the experimental and theoretical investigation of their electronic energy spectrum, structural configurations, and magnetic states, hold significant importance from both a fundamental and a practical standpoint. Heusler compounds, discovered over 100 years ago by German chemist F. Heusler [1], continue to be a subject of great interest in current research. These compounds exhibit a wide range of unique multifunctional properties [2], such as half-metallic ferromagnetism [3–5], spin gapless semiconductor state [6–8], topological insulator and semimetal behavior [8–11], shape memory effect [12,13], magnetocaloric effect [14,15], and many others (see, for example, [2,16,17] and references therein).

Among these materials, intermetallic compounds based on manganese, such as Mn_2YZ and Mn_3Z ($Y = V, Cr, Fe, Co, Ni$, etc.; $Z = Al, Ga, Ge, Sn$, etc.), are particularly noteworthy. In addition to the functional properties mentioned above, these compounds exhibit a range of unique magnetic characteristics, including the ability to manifest states of antiferromagnetism, compensated ferrimagnetism, and frustrated magnets. They possess unconventional magnetic

and electronic properties that are highly susceptible to external influences, making them promising candidates for practical applications in fields such as spintronics, microelectronics, and nanoelectronics.

Manganese-based Heusler compounds, specifically Mn_2YZ , possess several remarkable properties. They exhibit characteristics of half-metallic ferromagnets (HMF), spin gapless semiconductors (SGS), and potentially topological semimetals (TSM). These compounds also demonstrate a significant magnetocaloric effect and shape memory. Moreover, they offer the opportunity to realize unique magnetic states, including ferromagnetic (FM), antiferromagnetic (AFM), compensated ferrimagnetic (CFIM) ones, etc. (see, e.g., refs. [4,8,18]).

In previous studies, the intermetallic compounds Mn_3Z ($Z = Ge, Sn, Ga, Ir, Rh$) were found to exhibit a strong anisotropic anomalous Hall effect (AHE) and spin Hall effect in their antiferromagnetic state [19]. Researchers reported [20] a zero magnetic moment in thin films of the Mn_3Al alloy, which was attributed to a compensated ferrimagnetic state. This CFIM state differs from AFM due to the distinct crystallographic positions of manganese. Another study [21] observed a zero magnetic moment in the cast Mn_3Al alloy and suggested that it may also be indicative of compensated ferrimagnetism.

The combination of noncollinear magnetic structure and Berry curvature can result in a nonzero topological anomalous Hall effect, as demonstrated in antiferromagnets Mn_3Sn and Mn_3Ge [9,22]. These compounds, along with their noncollinear magnetic structures, also exhibit topological states in real space in the form of magnetic anti-skyrmions. The ability to manipulate the Berry curvature highlights the significance of understanding both the electronic and magnetic structures of Mn_3Z compounds.

Furthermore, among these intermetallic compounds, there are topological systems that possess unique surface states and display anomalous transport phenomena due to their unconventional bulk electronic topology. For instance, Mn_3Ge and Mn_3Sn compounds with a distorted $D0_{19}$ structure in the ab plane form a lattice of Mn atoms resembling a highly frustrated kagome lattice [22,23]. Further theoretical and experimental investigations of such structures and their impact on electronic and magnetic properties remain pertinent and in demand.

Figures 1–3 schematically show the models of an antiferromagnet and a compensated ferrimagnet (Figure 1), a half-metallic ferromagnet and a spin gapless semiconductor (Figure 2), and topological materials (Figure 3).

The magnetic structure of $D0_3$ compounds in the antiferromagnetic and compensated ferrimagnetic states is presented in Figure 1. As can be seen from Figure 1, the difference between antiferromagnetic and ferrimagnetic states is that the crystallographic positions of manganese with oppositely directed magnetic moments are completely different.

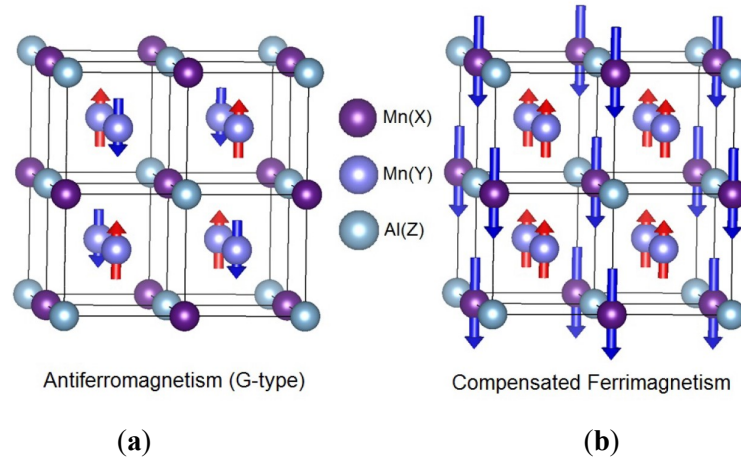


Figure 1. Schematic view of the magnetic structure of $D0_3$ compounds. **(a)** G-type antiferromagnetic structure of V_3Al , ions in $Mn(X)$ positions being nonmagnetic. **(b)** Magnetic structure of compensated ferrimagnet Mn_3Al [20]. Up-directed magnetic moments are shown by red arrows, and down-directed ones by blue.

Figure 2 shows the states of a half-metallic ferromagnet and a spin gapless semiconductor. The electronic structure of a half-metallic ferromagnet has the following features: there is a gap at the Fermi level for spin-down electronic states, which is absent for spin-up ones (Figure 2a). In the case of a spin gapless semiconductor (Figure 2b), the situation is similar, but there is a significant difference. As in a half-metallic ferromagnet, there is a finite gap for the spin-down spin projection, but the gap is zero for spin-up ones (Figure 2b). This is similar to the case of classical gapless semiconductors [24].

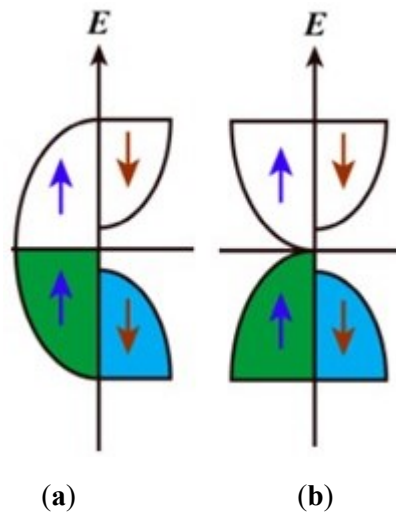


Figure 2. Simple models of half-metallic ferromagnets **(a)** and spin gapless semiconductors **(b)** [8]. The valence band for the electron states with spin up (blue arrows) is marked by green, and for ones with spin down (red arrows) by blue.

In topological materials (Figure 3), an inversion of the conduction and valence bands can occur because of a strong spin-orbit interaction. This leads to the appearance of a nontrivial topology of the electronic band structure, which is observed in topological insulators, Dirac and

Weyl semimetals. Topological insulators have a characteristic energy gap in bulk and “metallic” states on the surface (Figure 3a). The Dirac and Weyl semimetals also have a gap in the bulk resulting from strong spin–orbit coupling, except for the band intersection at Dirac (Figure 3b) and Weyl (Figure 3c) points, respectively.

The methods used to prepare intermetallic compounds, specifically those dealing with Mn_3Z , can have a significant impact on their structural properties (see, e.g., refs. [25–29]). This, in turn, influences their electronic and magnetic states. Understanding the role of the structural state in the formation and behavior of intermetallic compounds based on manganese is an important and fascinating problem.

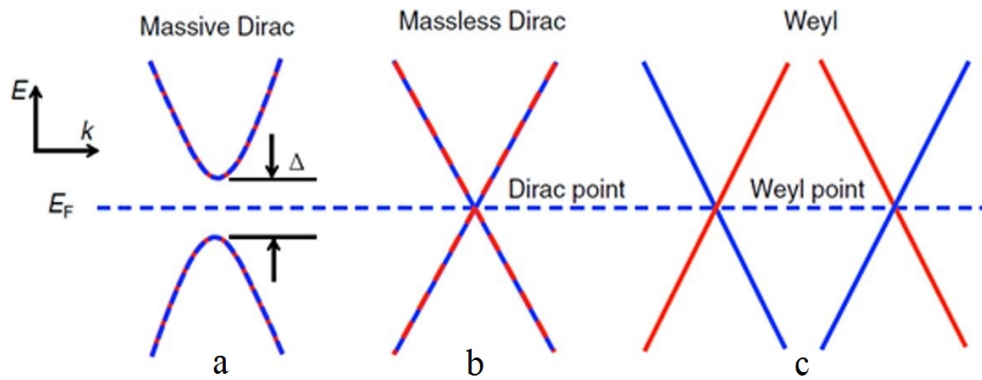


Figure 3. Schematic representation of the band structure of (a) massive Dirac, (b) “massless” Dirac, and (c) Weyl fermions. The latter arises during the decay of the Dirac point. Two-color and one-color curves and lines represent doubly degenerate and nondegenerate zones, respectively [8].

Both experimental and theoretical studies in this area hold great relevance and scientific significance (see papers [30–32] and references therein). They allow for a comprehensive description of the evolution of the electronic structure, magnetic state, and properties of Mn_2YZ and Mn_3Z compounds. These studies aim to understand the characteristics and differences in the manifestation of various states, such as antiferromagnetism, compensated ferrimagnetism, frustrated magnetism, half-metallic ferromagnetism, spin gapless semiconductors, topological semimetals, etc. This work provides a concise overview of the research on electron transport and the magnetic state in compounds based on manganese, specifically Mn_2YZ and Mn_3Z ($Y = Sc, Ti, V, Cr, Fe, Co, \text{etc.}; Z = Al, Ge, Sn, Si, Pt, \text{etc.}$).

2. Electronic and Magnetic Properties of Mn_2YZ ($Y = V, Cr, Fe, Co, Ni, \text{etc.}; Z = Al, Ge, Sn, Si, Pt, \text{etc.}$) Compounds

The HMF state was theoretically predicted in 1983 in ref. [33] using band calculations of the NiMnSb half-Heusler compound. Later, the HMF theory was significantly supplemented and

extended [3,34]. After 40 years, band calculations are still extensively used to predict the HMF state in various compounds (see, for example, refs. [4,5] and references therein).

Electronic structure calculations performed on manganese-based Heusler alloys have shown that many of them can exhibit HMF properties. These are Mn_2VZ ($Z = \text{Al, Ga, In, Si, Ge, Sn}$) compounds [35], Mn_2FeZ ($Z = \text{Al, Ga, Si, Ge, Sb}$) [36], Mn_2CrZ ($Z = \text{Al, Ga, Si, Ge, Sb}$) [37], Mn_2TiZ ($Z = \text{Al, As, Bi, Ga, Ge, Sb, Si, Sn}$) [38], Mn_2ZrZ ($Z = \text{Ga, Ge, Si}$) [39,40]. It is worth emphasizing that the HMF state predicted theoretically and/or as a result of band calculations is by no means always realized in real compounds.

Using density functional theory, the electronic, magnetic, and structural properties of ferrimagnetic Mn_2VAl and Mn_2VSi Heusler alloys were studied in ref. [41]. It was shown that two states can exist in studied compounds: one state with low magnetization and a HMF behavior with almost 100% spin polarization and the second state with high magnetization and a metallic character.

The temperature dependences of the electrical resistivity $\rho(T)$ of the Mn_2CrAl alloy were studied in [21]. It can be observed (see Figure 1 in ref. [21]) that the residual resistivity ρ_0 reaches a large value of $\approx 250 \mu\Omega \text{ cm}$, and the resistivity ρ decreases with temperature increasing up to room temperature. A similar behavior $\rho(T)$ was observed for Mn_2FeAl in [42]. The large values of ρ_0 and the “semiconductor” dependence $\rho(T)$ were explained by the structural disorder. There is a so-called Mooij rule [43], according to which in metallic systems with the static disorder, i.e., with resistivity $\rho > (150-200) \mu\Omega \text{ cm}$, a negative temperature coefficient of resistance is usually observed. The estimates of the concentration n of current carriers from measurements of the Hall effect give large values: $n \approx 1.6 \cdot 10^{22} \text{ cm}^{-3}$ for Mn_2CrAl [21], and $n \approx 2 \times 10^{22} \text{ cm}^{-3}$ for Mn_2FeAl [42].

Studies of the magnetic properties of Mn_2CrAl [21] and Mn_2FeAl [42,44] alloys showed that the behavior of the magnetization $M(H)$ indicates a total moment close to zero (see, e.g., Figure 4). Such a state can be characterized as (1) a compensated ferrimagnet, which retains the nature of a half-metallic ferromagnet state [20,45], or as (2) an antiferromagnet.

The distinction between them can be explained as follows. In the case of antiferromagnetism, the opposite magnetic moments of manganese are situated in positions that are equivalent from a crystallographic perspective. Conversely, in the case of compensated ferrimagnetism, these opposite moments of manganese occupy crystallographically distinct positions. In CFIM, the compensation of magnetic moments is not solely reliant on crystal symmetry but is also influenced by a unique band structure. The utilization of CFIM and/or AFM states in such materials holds promise for applications in spintronics as they can exhibit high spin polarization of current carriers.

It is shown in ref. [44] that a frustrated antiferromagnetic state is observed in Mn_2FeAl alloy with a Neel temperature $T_N = 48$ K and a Curie–Weiss temperature $\theta_{\text{CW}} \approx -230$ K. In this case, large antiferromagnetic spin fluctuations, caused by the geometric frustrations, lead to the appearance of an unusually large electronic heat capacity. According to ref. [44], the corresponding value of the T -linear heat capacity coefficient is $\gamma = 210$ mJ/molK².

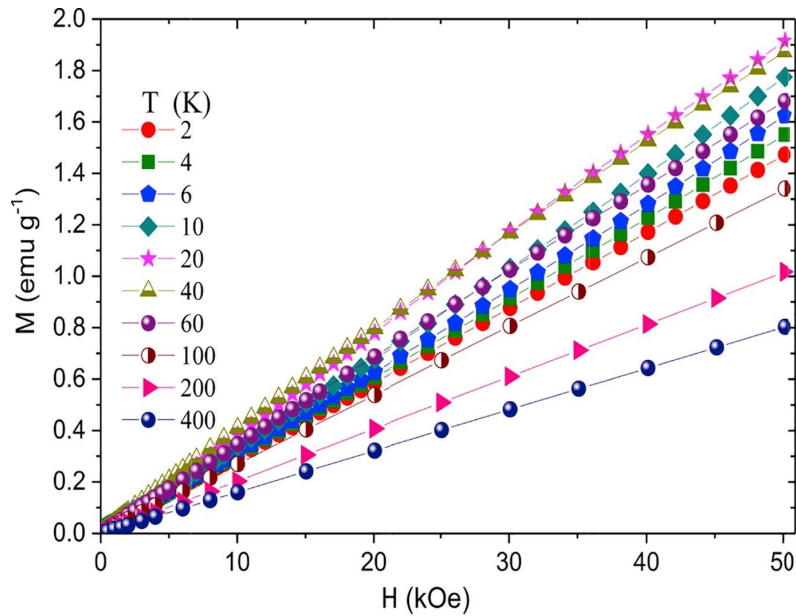


Figure 4. Field dependence of magnetization for Mn_2FeAl at different temperatures [42].

The Mn_2CoAl compound exhibits even higher residual resistivity values [46,47] (Figure 5), belonging to a novel class of quantum materials known as spin gapless semiconductors. The theoretical prediction of SGS materials was made in 2008 [6]. SGS materials possess an unusual band structure, wherein there exists an energy gap for the spin-down electron subsystem near the Fermi level, while the spin-up electronic states have the top of the valence band touching the bottom of the conduction band. Under these circumstances, the kinetic properties of SGS materials are expected to resemble those of “classical” gapless semiconductors [24], including high residual resistivity with weak temperature dependence, relatively low current carrier concentration, and low thermoelectric power. Due to the prevalence of spin-up current carriers, a high degree of spin polarization, a significant magnetization, and an anomalous Hall effect are anticipated. Experimental evidence of this spin gapless semiconductor state with unusual magnetic and magnetotransport properties has been observed in Mn_2CoAl [46,47] and Ti_2MnAl Heusler alloys [48].

Figure 5 shows the temperature dependencies of the electrical resistivity, the Seebeck coefficient, and the concentration of current carriers of the Mn_2CoAl compound [47]. It can be seen that the residual resistivity is very large and amounts to ~ 445 $\mu\Omega$ cm, and the resistivity itself slightly decreases with temperature, reaching a value of ~ 410 $\mu\Omega$ cm at room temperature.

In this case, the thermoelectric power is small and weakly changes with temperature. Finally, the concentration of charge carriers is relatively low, monotonically increasing with temperature: $n \approx 1.65 \times 10^{20} \text{ cm}^{-3}$ at 2 K and $\sim 3 \times 10^{20} \text{ cm}^{-3}$ at room temperature. Finally, measurements of the Hall effect in Mn_2CoAl [47] show that the value of the anomalous Hall conductivity σ_{xy} is relatively small and at 2 K is $\sigma_{xy} = 21.8 \text{ S cm}^{-1}$, which can be explained by the symmetry features of the Berry curvature (Figure 5). These facts confirm the realization of the state of a spin gapless semiconductor in the Mn_2CoAl compound.

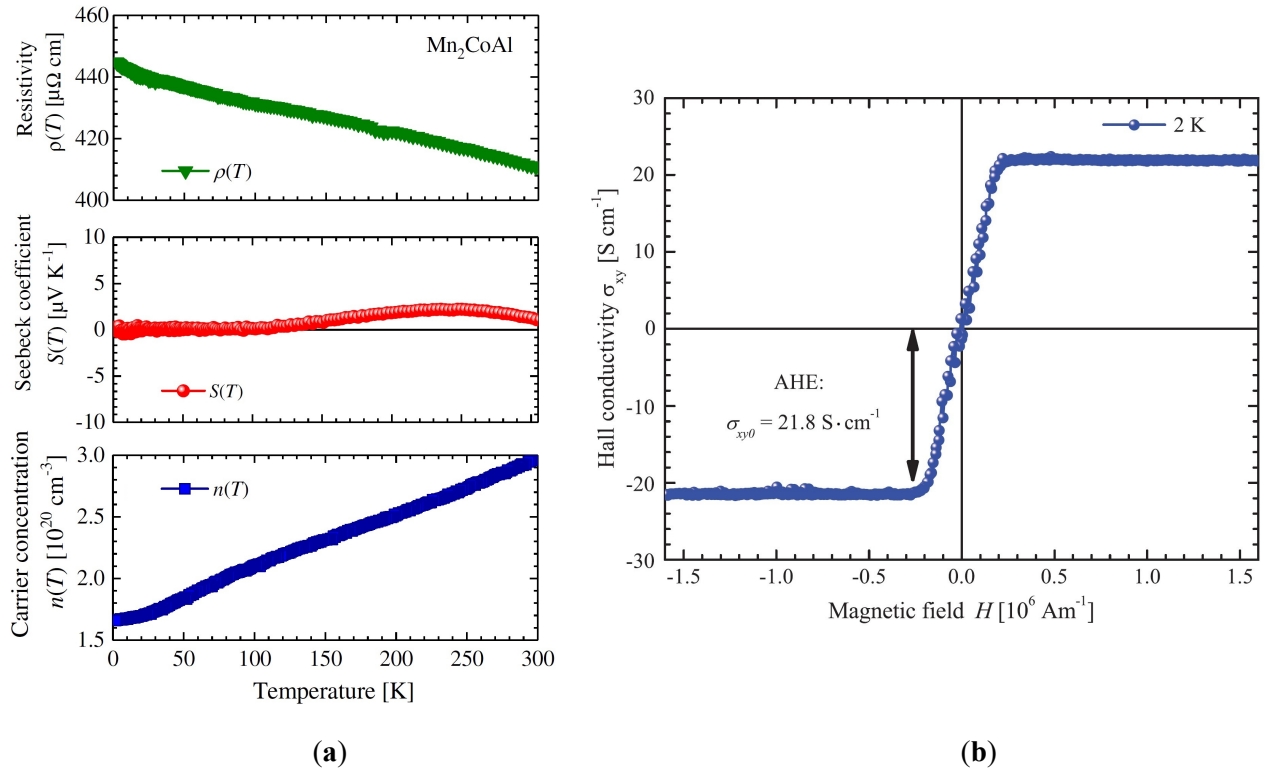


Figure 5. Mn_2CoAl compound [47]. (a) Temperature dependence of the electroresistivity ρ , Seebeck coefficient S , and charge carriers concentration n . (b) Field dependence of Hall conductivity at $T = 2 \text{ K}$.

It is important to highlight that the characteristics of a spin gapless semiconductor (SGS) are not limited to electron transport but also extend to other properties, including optical characteristics. In a study referenced as [49], the optical properties of the Mn_2CoAl compound, which exhibits SGS behavior, were investigated. The study also involved the calculation of its electronic structure. The findings revealed distinct optical properties of Mn_2CoAl , including positive values of the real part of the dielectric constant (ϵ_1) and the absence of the Drude contribution to the optical conductivity in the infrared (IR) region of the spectrum within the examined range. These observations suggest a slight deviation or “deterioration” of the metallic properties of Mn_2CoAl .

Besides, the authors of the study observed [49] intense interband absorption in the IR range and concluded that the band spectrum had a complex structure with a high density of d -states near the Fermi level E_F . The observed features of the optical properties allowed the authors [49] to explain the band spectrum characteristic of spin gapless semiconductors.

The electronic structure and magnetic properties of Heusler alloys, specifically Mn_2YZ , can be significantly altered by modifying their composition through the substitution of atoms and applying external influences, like hydrostatic pressure and mechanical processing. In ref. [50], the authors investigated the structure, mechanical, electronic, and magnetic properties of $Mn_{2-x}Fe_{1+x}Si$ Heusler alloys (where $x = 0, 0.25, 0.5, 0.75, 1$) using density functional theory. By replacing Mn atoms with Fe atoms, it was observed that all the studied alloys maintain mechanical and dynamic stability, adopting the Hg_2CuTi structure for $x = 0, 0.25$ and 0.5 and the Cu_2MnAl structure for $x = 0.75$ and 1 . Furthermore, as the iron content increases, the alloys exhibit improved ductility. All the studied alloys display half-metallic ferromagnetic behavior, with the Fermi levels gradually shifting toward the middle of the bandgap in the spin-down direction with increasing iron content.

In the study [51], researchers successfully synthesized the Mn_2FeSi Heusler alloy using a high-energy planetary ball mill. The resulting compound was found to be an inverse Heusler alloy with an X_A structure. Through the use of Mössbauer spectroscopy and magnetization measurements, they discovered that the synthesized material exhibits a heterogeneous magnetic structure at room temperature. This structure is composed primarily of the paramagnetic phase, with small contributions from ferro- and ferrimagnetic phases. The Neel temperature $T_N = 67$ K was determined from the temperature dependences of the magnetization.

Using ab initio calculations and the Monte Carlo simulation method in [52], the structural, magnetic, and electronic properties of Mn_2YSn ($Y = Sc, Ti, \text{ and } V$) Heusler alloys were studied under applied hydrostatic pressure. The coexistence of two magnetic states with a low and a high magnetic moment was found for a small and large volume of the crystal lattice, correspondingly. These states coexist together due to almost equal energy at an applied pressure of 3.4, -2.9, and -3.25 GPa for Mn_2ScSn , Mn_2TiSn , and Mn_2VSn , respectively. A positive pressure corresponds to a uniform compression of the lattice, and a negative one corresponds to a uniform expansion of the lattice. It was demonstrated that for the studied compounds, the low-magnetic state (LMS) was characterized by an almost half-metallic behavior, while the high-magnetic state (HMS) acquired a metallic character. It was shown that the parameters of magnetic exchange and Curie temperatures were significantly higher for the HMS than for the LMS. The authors proposed a mechanism for switching between the half-metallic state with the LMS and the metallic state with the HMS using applied pressure.

In addition to the electronic and magnetic states discussed above, Heusler alloys based on manganese can exhibit other thermodynamic phenomena, such as the shape memory effect and the magnetocaloric effect. Moreover, unlike the well-known Heusler-like alloys based on Ni-Mn-Z ($Z = \text{Ga, In, Sn, etc.}$) with strong deviations from stoichiometry (of the type $\text{Ni}_{2\pm x}\text{Mn}_{1\pm x}\text{Z}$), SME and MCE can also be observed in full Heusler alloys Mn_2YZ , where $Y = \text{Sc, Ti, V, Co, Ni, etc.}$; $Z = \text{Ga, Ge, Sn, etc.}$ (see, e.g., [53–55] and references therein).

Similar magnetic and electronic states can be realized in binary intermetallic compounds based on manganese Mn_3Z ($Z = \text{Al, Ge, Ga, etc.}$) as well.

3. Features of the Electronic Transport and Magnetic State of Mn_3Z ($Z = \text{Al, Ge, Si, Sn, Pt, etc.}$) Compounds

Compensated ferrimagnets possess a magnetic moment that totals zero, but their density of electronic states for opposite spin directions allows for a significant spin polarization of current carriers. A study [20] indicates that the compensated ferrimagnetic state is present in Mn_3Al , and this half-metallic state can persist at room temperature. In the same study, the magnetic properties of thin films of Mn_3Al were examined. The results reveal that the films demonstrate the state of a compensated ferrimagnet, with a total magnetization value of $M = 0.11 \pm 0.04 \mu_{\text{B}}/\text{f.u.}$

Results [20] are in good agreement with refs. [28,29] where the electronic transport and magnetic characteristics of cast and rapid melt-quenched (RMQ) Mn_3Al alloys were measured and compared.

In Figure 6, the field dependence of the magnetization ($M = f(H)$) is shown for both the cast and RMQ alloy Mn_3Al at a temperature of 4.2 K, as described in reference [29]. It can be observed from Figure 6a that the cast alloy exhibits a small magnitude of magnetization, which increases linearly with the applied field. At a field strength of 70 kOe, the magnetization reaches approximately 1.1 emu/g. In contrast, the Mn_3Al RMQ alloy (Figure 6b) displays a significantly different shape of the $M(H)$ dependence. In this case, even in weak magnetic fields, there is an increase in magnetization, followed by a tendency toward saturation.

In ref. [29], the difference in $M(H)$ behavior for Mn_3Al is explained as follows. In the case of a cast compound having the β -Mn structure, a frustrated antiferromagnetic state can arise, which manifests itself in the $M(H)$ dependences (Figure 6a) and in the temperature dependences of the susceptibility (Figure 7). The results obtained in [29] are in good agreement with the conclusions of ref. [42] obtained on Mn_2FeAl with the same β -Mn structure.

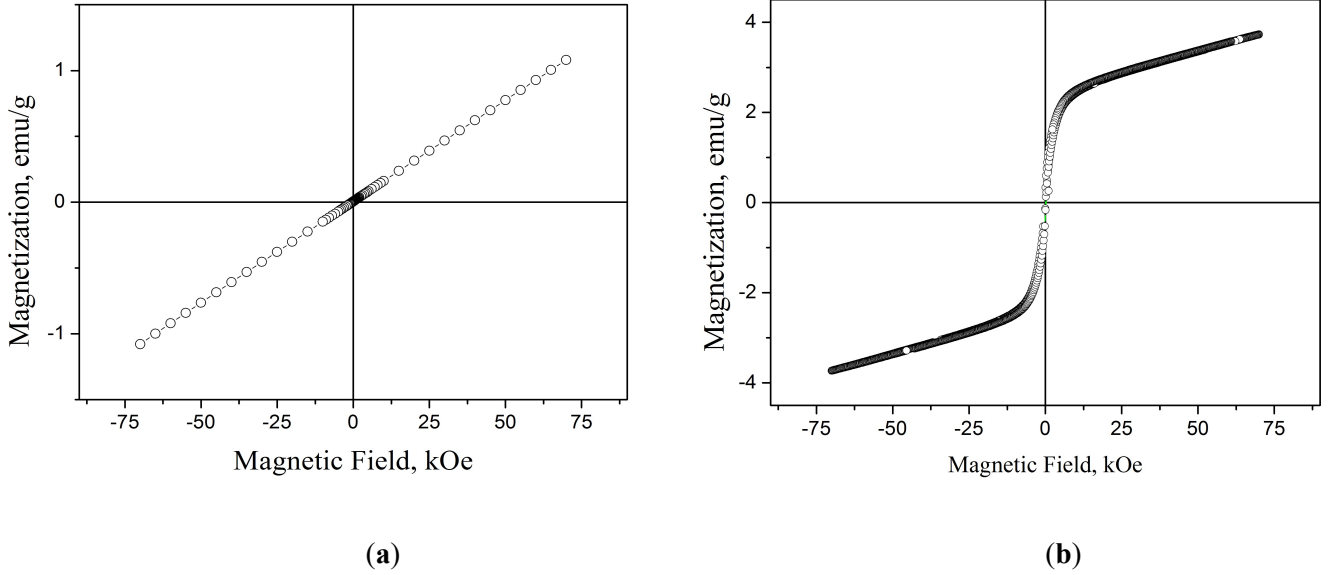


Figure 6. Field dependence of magnetization for Mn₃Al at $T = 4.2$ K: (a) cast and (b) RMQ samples [29].

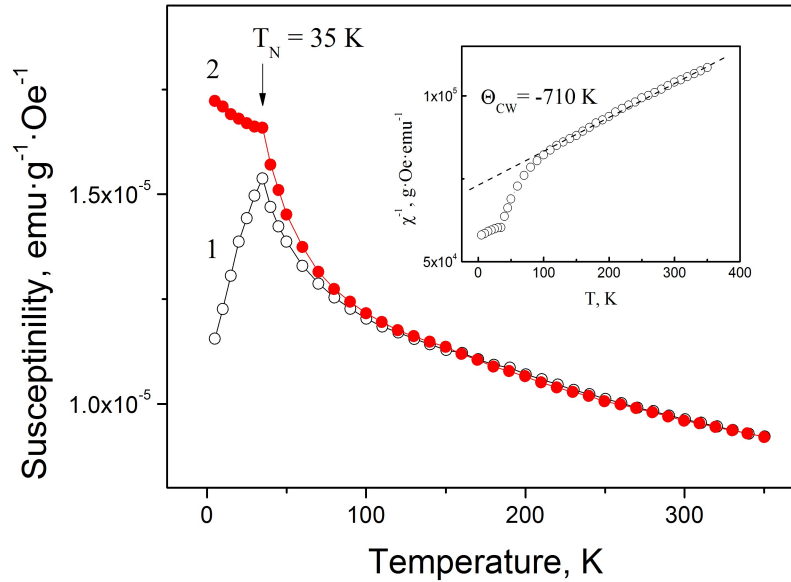


Figure 7. The magnetic susceptibility of the Mn₃Al alloy measured at a magnetic field strength of 100 Oe during the cooling process. The results are represented by two sets of data points: (1) open circles that indicate measurements conducted without the application of a magnetic field and (2) solid red circles that correspond to the presence of a magnetic field. The inset shows the temperature dependence of the inverse magnetic susceptibility χ^{-1} [29]. The Curie–Weiss law with the temperature $\theta_{CW} \approx -710$ K is shown by dashed line.

According to ref. [29], a decrease in grain size and an increase in “disorder” are observed in Mn₃Al after RMQ treatment. As shown in [56], the magnetic state of the Mn₃Al alloy is very sensitive to the filling of interstices and degree of ordering. According to first-principles calculations [18] in Mn₃Al with the $D0_3$ structure, a compensated ferrimagnetic state with a zero

moment can arise, which is observed in the RMQ compound Mn_3Al (Figure 6b) according to [29].

Figure 7 displays the temperature dependence of the susceptibility for the Mn_3Al alloy [29]. The inset graph illustrates the temperature dependence of the inverse susceptibility at a magnetic field strength of 100 Oe. At high temperatures, the data approximately follow the Curie–Weiss law with a temperature θ_{CW} of around -700 K. This behavior suggests the possible presence of an antiferromagnetic state. The Neel temperature T_{N} can be estimated by observing the point where the magnetic susceptibility curve breaks. In our case, T_{N} is determined to be 35 K (as shown in Figure 7). The large ratio $|\theta_{\text{CW}}|/T_{\text{N}}$ indicates a frustrated antiferromagnetism in the cast Mn_3Al compound [29].

The cast and RMQ alloys investigated in [28,29] have the β -Mn structure. This consists of two distinct sublattices, one of which is made up of triangles arranged perpendicular to the [111] axes and forming a three-dimensional kagome-like lattice. Recent experimental studies have shown that in systems with strong frustration caused by competing exchange interactions, not only a quantum state of spin liquid can arise, but also antiferromagnetism with a significantly reduced, but still finite, Neel temperature can occur. These systems are characterized by a frustration parameter, the ratio $|\theta_{\text{CW}}|/T_{\text{N}}$; in the intermediate temperature range $T_{\text{N}} < T < |\theta_{\text{CW}}|$, the system can exhibit unusual spin-liquid properties. High values of the frustration parameter have been observed in the PdCrO_2 compound where $T_{\text{N}} = 37$ K and $\theta_{\text{CW}} \approx -500$ K [57]. This behavior is not explained by the standard Heisenberg model and is thought to be due to correlation effects in the subsystem of itinerant electrons [58]. A similar behavior of the magnetic susceptibility was recently discovered in the Mn_2FeAl compound with the β -Mn structure in [42,44] ($T_{\text{N}} = 42$ K, $\theta_{\text{CW}} \approx -230$ K according to [44]).

According to calculations [56], the Mn_3Al compound in the β -Mn structure exhibits a ferrimagnetic state, where the magnetic moment of the sublattices is not significantly compensated. However, ab initio calculations [20,59] in the $D0_3$ structure suggest that a compensated ferrimagnetic state with a zero moment and a half-metallic structure arises. The results from [60] are not fully supported by experimental data [28,29]. These data suggest that both the cast and RMQ Mn_3Al alloys exhibit a frustrated antiferromagnetic state and an almost compensated ferrimagnetic state, respectively. In the case of a cast Mn_3Al alloy with the β -Mn structure, the absence of a long-range magnetic order can manifest itself as the Hall effect in the form of a zero anomalous contribution. On the contrary, in the case of the RMQ alloy with the β -Mn structure in the state of a compensated ferrimagnet, an anomalous Hall effect should be observed.

Figure 8 illustrates the temperature dependence of the electrical resistivity $\rho(T)$ for cast and rapidly melt-quenched Mn_3Al alloys [29]. In the cast alloy (Figure 8a), it can be observed that the residual resistivity ρ_0 is relatively high, reaching a value of approximately $307 \mu\Omega \text{ cm}$. The resistivity follows a semiconductor-like trend, decreasing with increasing temperature. However, after quench hardening (Figure 8b), there is a significant reduction in the residual electrical resistivity ρ_0 by more than an order of magnitude, down to $12 \mu\Omega \text{ cm}$. Additionally, a minimum point appears on the temperature dependence $\rho(T)$ at around 60 K.

Typically, rapid melt quenching results in the formation of fine-grained structures, which can lead to increased resistivity due to the scattering of current carriers at grain boundaries. However, this phenomenon was not observed in the Mn_3Al alloy studied [28,29]. Instead, the presence of manganese sulfide (MnS) precipitates at the grain boundaries occurred, explaining the high electrical resistivity values in the cast alloy. The rapid melt-quenching process caused the dissolution of manganese sulfide within the volume of the grains, resulting in grain boundaries free of MnS. As a result, the resistivity of the rapidly melt-quenched alloy decreased compared with the cast alloy. Similar behavior was also observed in the Hall effect measurements [28,29].

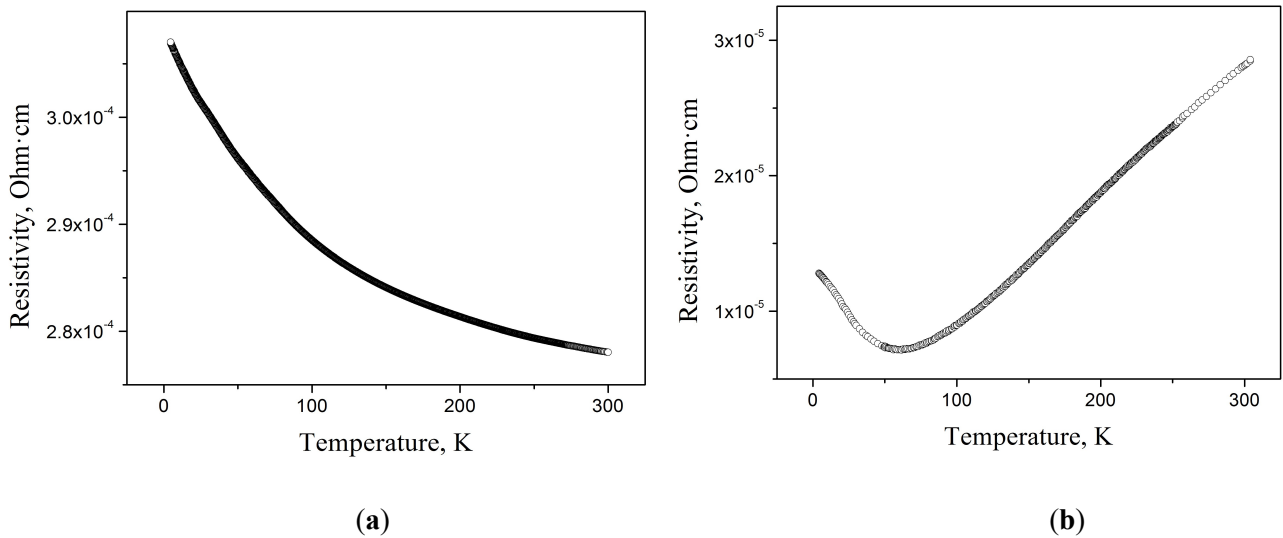


Figure 8. Temperature dependence of the resistivity for cast (a) and RMQ (b) Mn_3Al [29].

Figure 9 shows the dependence of the Hall resistivity $\rho_{xy} = f(H)$ at $T = 4.2 \text{ K}$ for the cast and RMQ Mn_3Al alloy. In the first case, a linear increase in ρ_{xy} is observed, and in the second case, the behavior of $\rho_{xy}(H)$ is typical for alloys with an anomalous Hall effect [28,29]. These data also indicate the absence of spontaneous magnetization in the case of cast Mn_3Al and the realization of a compensated ferrimagnet state in the RMQ Mn_3Al alloy [28,29].

Traditionally, it was believed that the anomalous Hall effect (AHE) was exclusive to ferromagnetic materials [61]. However, it has been discovered that the AHE can manifest in

various magnetic materials as a result of broken time-reversal symmetry. In reference [62], ab initio calculations were conducted, taking into consideration the symmetry properties of the nontrivial AHE in the Mn_3Al compensated ferrimagnet. The nonzero elements of the anomalous Hall conductivity were determined based on the magnetic space group of Mn_3Al . The calculations revealed that the value of the anomalous Hall conductivity was $\sigma_{xy} = -320 (\Omega \text{ cm})^{-1}$. The study also delved into the nature of the Berry curvature, which is responsible for the internal origin of the AHE, using group theory. Furthermore, the overall behavior of the Berry curvature across the entire Brillouin zone was illustrated.

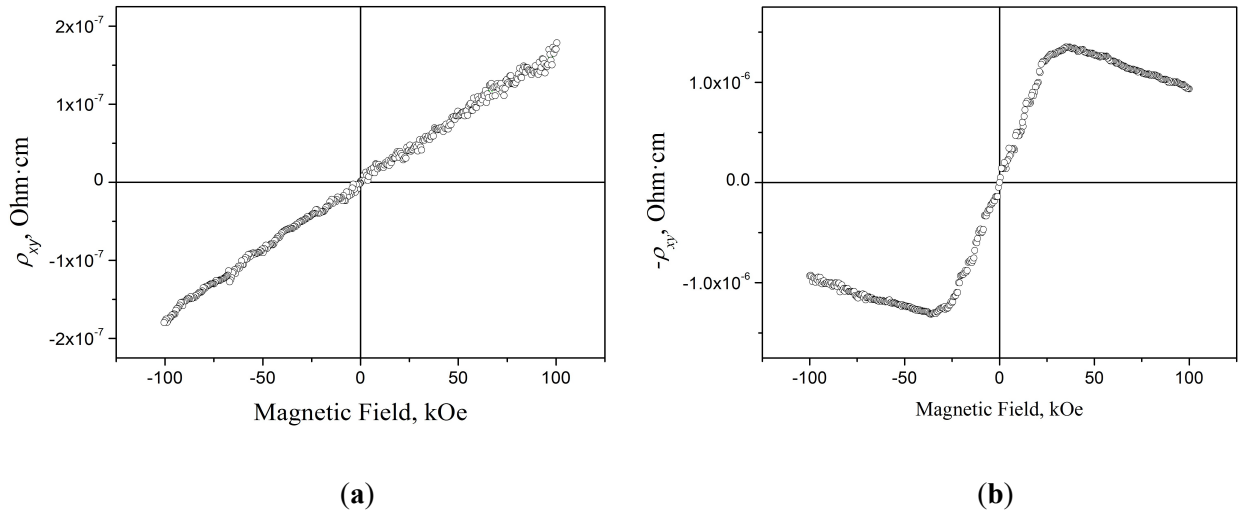


Figure 9. Field dependence of Hall resistivity for Mn_3Al at $T = 4.2 \text{ K}$ [29]: (a) cast and (b) RMQ samples.

The observation of a nonzero topological anomalous Hall effect in antiferromagnets Mn_3Sn and Mn_3Ge [9] can be attributed to their noncollinear magnetic structure and Berry curvature. A study conducted in [63] focused on the magnetization and anomalous Hall effect of a single-crystal hexagonal chiral antiferromagnet Mn_3Ge . Remarkably, it was discovered that this material exhibited a significant anomalous Hall conductivity of approximately $60 (\Omega \text{ cm})^{-1}$ at room temperature and $\sim 380 (\Omega \text{ cm})^{-1}$ at 5 K in zero field, approaching half the anticipated value for a quantum Hall effect on an atomic layer with a Chern number of one. Furthermore, the sign of the anomalous Hall effect was found to change with a magnetic field vector direction change of less than 0.1 T or with a rotation of a small magnetic field of less than 0.1 T. This intriguing behavior could have implications in the development of switching and storage devices based on antiferromagnets.

It is worth noting that recent studies have reported new antiferromagnetic materials with rapid response times, low power consumption, and high immunity to external magnetic fields. These materials show promise in the field of spintronics [64–69].

In materials exhibiting noncollinear antiferromagnetism, the magnetic moments of atoms are not strictly aligned along a single axis. One such material is Mn_3Ge , which falls into the category of noncollinear antiferromagnetic materials. In Mn_3Ge , the manganese atoms form a hexagonal sublattice, and their magnetic moments arrange themselves in a kagome lattice structure (Figure 10). This unique arrangement gives rise to a noncollinear antiferromagnetic state and several other unusual effects, including a large anomalous Hall effect, a new spin Hall effect, and a significant spin Nernst effect [70–72].

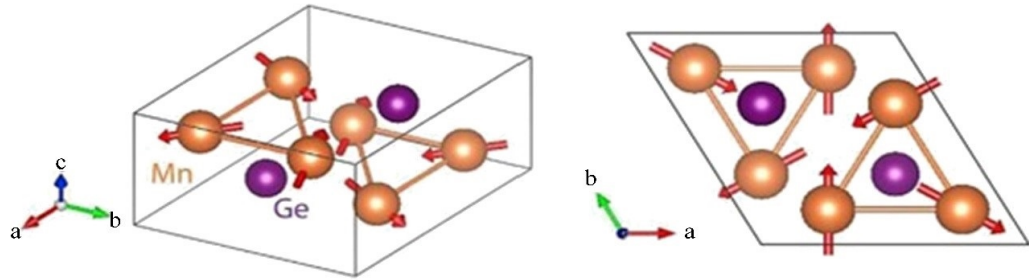


Figure 10. $D0_{19}$ structure for Mn_3Ge . Red arrows show the Mn magnetic moments [23].

A study conducted in [73] focused on the magnetic structure of antiferromagnetic Mn_3Ge crystals with a kagome lattice, using polarized neutron diffraction. The study has revealed that in Mn_3Ge , the magnetic order is characterized by a coplanar state represented by $\mathbf{k} = 0$, which belongs to the two-dimensional irreducible representation of the double group Γ_9 , which is the only irreducible representation consistent with the observed diffraction pattern of Mn_3Ge [73]. This coplanar state exhibits a perfect 120° antichiral structure with an angle of 120° and a magnetic moment of $2.2 \mu_B/\text{Mn}$. Additionally, a weak collinear ferromagnetism is observed. A phenomenological spin Hamiltonian is proposed to describe the manganese-based magnetism, incorporating exchange interactions, Dzyaloshinskii–Moriya interactions, and single-ion crystal field terms. These interactions contribute to spin wave damping and an extended range of magnetic interactions indicate an itinerant magnetism compatible with anomalies of transport properties.

In [74], a study was conducted on the electrical, magnetic, galvanomagnetic, and thermal properties of a single crystal of the noncollinear antiferromagnet Mn_3Ge . The researchers discovered that at very low temperatures, the Wiedemann–Franz law, which establishes a connection between the electronic and thermal Hall effects, holds true. However, deviations from this law were observed at temperatures above 100 K. The investigation revealed that the carriers in Mn_3Ge have a short mean free path, similar to the distance between Mn antisite defects. As a result, the elastic scattering of current carriers becomes the dominant factor. The researchers

proposed that the deviation from the Wiedemann–Franz law is attributed to a disparity between the thermal and electrical contributions of the Berry curvature along the Fermi surface. Theoretical calculations supported this interpretation, demonstrating that the Berry spectra in the two systems are not identical. Importantly, the study also confirmed that the Bridgman relation, which links the anomalous Nernst and Ettingshausen coefficients, is valid across the entire temperature range investigated.

External pressure and doping can alter the Berry curvature, as well as the corresponding physical properties. In a study [75], the anomalous Hall effect in a single crystal of antiferromagnetic Mn_3Ge was investigated under hydrostatic pressure up to 2.85 GPa. It was observed that the Hall signal becomes zero at a pressure of 1.53 GPa, and changes sign at higher pressures. Although the sign of the Hall conductivity changes with increasing pressure, its saturation value at room temperature remains relatively high, around $23 (\Omega \text{ cm})^{-1}$ at 2.85 GPa, which is comparable to the saturation value at atmospheric pressure $40 (\Omega \text{ cm})^{-1}$. The authors suggest that this change in the Hall conductivity may be attributed to gradual modifications in the in-plane components of the Mn moments within a noncollinear triangular magnetic lattice. These findings provide insights into the possibility of manipulating and controlling the anomalous Hall effect in chiral antiferromagnetic Mn_3Ge through pressure-induced changes.

Authors of [76] investigated the magnetic and electronic structure of the $(\text{Mn}_{0.78}\text{Fe}_{0.22})_3\text{Ge}$ hexagonal single crystal, which is known as a Weyl semimetal, using electron transport, magnetic properties, and neutron diffraction experiments. The researchers conducted temperature measurements of the magnetization and observed two magnetic transitions at $T_{\text{N}1} = 242 \text{ K}$ and $T_{\text{N}2} = 120 \text{ K}$. In this case, the anomalous Hall effect is observed in the intermediate range at temperatures between $T_{\text{N}1}$ and $T_{\text{N}2}$, disappearing at $T < T_{\text{N}2}$. Neutron diffraction experiments were carried out to determine the magnetic structures of the $(\text{Mn}_{0.78}\text{Fe}_{0.22})_3\text{Ge}$ single crystal. Neutron diffraction studies made it possible to conclude that the sample has a collinear antiferromagnetic structure below the temperature $T_{\text{N}2}$. In this case, the magnetic structure is noncollinear antiferromagnetic in the intermediate temperature range. The authors conclude that the observation of an anomalous Hall effect and a noncollinear magnetic structure in $(\text{Mn}_{0.78}\text{Fe}_{0.22})_3\text{Ge}$ in this temperature range indicates the existence of Weyl points. At temperatures below $T_{\text{N}2}$, there is no anomalous Hall effect, and the magnetic structure changes to a collinear antiferromagnetic one. This indicates a strong coupling between the magnetic and electronic structures of the $(\text{Mn}_{0.78}\text{Fe}_{0.22})_3\text{Ge}$ compound.

The influence of pressure, reaching up to 2.2 GPa, on the electrical resistivity ρ and thermoelectric power S of the Mn_3Si single-crystal compound was investigated in a study referenced as [77]. The Neel temperature T_{N} was determined by analyzing the temperature

dependencies of ρ and S , revealing an increase in T_N with rising pressure. Notably, the resistivity and thermoelectric power displayed significant changes at around $P \approx 1$ GPa at a temperature of 2 K, indicating the occurrence of a phase transition.

Another research, referenced as [78], presents findings on the structural and magnetic properties of noncollinear antiferromagnetic Mn_3Sn films that adopt the $D0_{19}$ hexagonal structure. These films were observed to exhibit weak ferromagnetism, characterized by an uncompensated in-plane magnetization of 34 kA/m and a coercive force $\mu_0 H_c$ of 4.0 mT at room temperature. Additionally, the study investigated the phenomenon of exchange bias in $\text{Mn}_3\text{Sn}/\text{Py}$ bilayers, revealing the potential to achieve exchange bias fields of up to $\mu_0 H_{\text{EB}} = 12.6$ mT at 5 K. These results highlight the attractiveness of Mn_3Sn films for applications in antiferromagnetic spintronics.

A study in [79] reports on the unusual behavior of the anomalous Hall effect in the compound Mn_3Sn . The authors discovered a linear dependence on the magnetic field, which they attributed to the Berry curvature of the wave function. Interestingly, the magnitude of the Hall signal in this case exceeds what would be expected in the semiclassical model. The authors propose that the magnetic field induces a nonplanar spin canting, resulting in a nontrivial chirality of the spins on the kagome lattice. This leads to changes in the band structure, specifically gapping out previously unknown Weyl nodal lines, which explains the observed behavior of the anomalous Hall effect. The findings suggest a connection between the Berry phase in real space, arising from spin chirality, and the curvature of the Berry momentum space in the kagome lattice.

The paper [80] investigates the electronic transport and magnetic properties of Mn_3Sn films. The findings reveal that these films exhibit a weak uncompensated magnetic moment of approximately $0.12 \mu_B/\text{f.u.}$ and an electrical resistance of about $3.8 \mu\Omega \text{ m}$ at room temperature. These results closely match the data obtained for bulk Mn_3Sn , indicating high purity and perfection in the synthesized films, with a resistance ratio RRR of 3.92. The Mn atoms in the Mn_3Sn compound are arranged in a kagome-type lattice. The study demonstrates that at room temperature when the external magnetic field is perpendicular to the kagome planes, a weak anomalous Hall effect is observed along with a Hall resistance that varies linearly with the field. The researchers identify three distinct magnetic phases in the investigated films of the chiral antiferromagnet Mn_3Sn : an inverse triangular spin state occurring above 250 K, a helical phase stabilized between 100 and 250 K, and a spin glass phase formed below 100 K. Based on their findings, the authors suggest that these films may support topologically protected skyrmions, where the fictitious effective magnetic field is estimated to be around 4.4 T. This indicates the potential for unique magnetic phenomena in the Mn_3Sn films.

Currently, there is active research on the physics of Berry curvature and related nontrivial magnetic transport in two-dimensional spin-lattice kagome structures of noncollinear antiferromagnets. The focus has mainly been on hexagonal chiral antiferromagnets like Mn_3Sn , while studies on face-centered cubic (fcc) noncollinear antiferromagnetism are limited. One such example of fcc noncollinear antiferromagnets is Mn_3Pt .

In reference [81], the researchers examined single crystals of Mn_3Pt . They discovered that applying uniaxial stress to Mn_3Pt crystals decreased their coercive force. This allowed them to observe the anomalous Hall effect in bulk materials of the Mn_3Z family with a cubic structure. Interestingly, the anomalous Hall effect remained even after the stress was removed, suggesting that stress-induced ferromagnetic moments had minimal impact on the effect. The study found that longitudinal stress reduced the coercive force more than transverse stress, indicating that the dominant response to applied stress was a rotation of spins within the plane. However, further investigation is needed to verify this assumption, particularly through direct observation of piezomagnetism.

In reference [82], the authors systematically studied the effect of deformation on the magnetic properties and the anomalous Hall effect of fcc noncollinear antiferromagnetic Mn_3Pt films. They found that the ferromagnetic characteristics of Mn_3Pt films showed a similar response to strain, in contrast to hexagonal chiral antiferromagnets. The ferromagnetic signal in these films was attributed to the magnetic moment slope of Mn atoms in kagome structures, while the anomalous Hall resistivity was linked to the nonzero Berry curvature. By adjusting the thickness of the Mn_3Pt film, they achieved an anomalous Hall conductivity exceeding $100 (\Omega \text{ cm})^{-1}$. Additionally, the relationship between the Berry phase, magnetic properties, and AHE in Mn_3Pt was confirmed through a study on crystal growth orientation. The researchers concluded that this compound holds promise as a candidate for room-temperature antiferromagnetic spintronics.

4. Physical Mechanisms of the Magnetic States Formation in Mn-Based Compounds: Half-Metallic Ferromagnets and Spin Gapless Semiconductors

The existence of distinct spin-up and spin-down states in half-metallic ferromagnets presents a complex challenge to the general theory of itinerant magnetism [34]. The process of achieving a half-metallic state in Heusler alloys like $X\text{MnZ}$ and $X_2\text{MnZ}$, which have $C1_b$ and $L2_1$ structures, can be explained as follows [33,34,83,84]. When we disregard the hybridization of atomic states X and Z , the d band of manganese displays a significant energy gap between bonding and antibonding states. In a ferromagnetic state, the strong intra-atomic exchange (Hund's exchange) among manganese ions results in a notable separation of spin subbands for

up and down spins. One of these spin subbands closely interacts with the ligand's p band, leading to a partial or complete blurring of the corresponding energy gap due to p - d hybridization. Meanwhile, in the other spin subband, the energy gap remains intact and has the potential to align with the Fermi level, thus giving rise to the HMF state.

The $C1_b$ structure exhibits a real energy gap, whereas the $L2_1$ structure has a pronounced pseudogap. This difference is attributed to significant alterations in p - d hybridization, particularly between the p and t_{2g} states, in the absence of an inversion center, which is a characteristic feature of the $C1_b$ structure. As a result, the $C1_b$ structure is more favorable for the formation of the HMF state. The stability of the ferromagnetic state is a result of variations in p - d hybridization between states with opposite spin orientations, as elaborated in [84].

In a study [85], researchers conducted calculations for 54 ternary Heusler compounds with the composition X_2YZ . In this context, X represents a $3d$ transition metal (specifically Mn, Fe, Co), while Y and Z represent elements Y, Zr, Nb, Mo, Tc, Ru, Rh, Pd, Ag, and Al and Si, respectively. The findings from this study revealed that seven of these compounds—namely, Mn_2NbAl , Mn_2ZrSi , Mn_2RhSi , Co_2ZrAl , Co_2NbAl , Co_2YSi , and Co_2ZrSi —displayed 100% spin polarization, which classifies them as half-metallic ferromagnets (HMFs). Furthermore, five other alloys, specifically Mn_2TcAl , Mn_2RuAl , Mn_2NbSi , Mn_2RuSi , and Fe_2NbSi , exhibited high spin polarization levels (above 90%) with a gap present for one of the spin directions near the Fermi level. These alloys were categorized as “almost HMF” in the study [85]. Importantly, their Fermi levels were found to shift under pressure, resulting in the alignment of the Fermi level with the gap and the emergence of the HMF state.

An intriguing development in the field of half-metallic magnetism is represented by electron-deficient full Heusler alloys. Reducing the number of valence electrons to 24 per formula unit leads to either a nonmagnetic semiconductor or a half-metallic antiferromagnet. Remarkably, the reduction in the number of valence electrons can continue, entering a range of half-metals but with a bandgap for the majority spin direction. This is best exemplified by the case of Mn_2VAl , which is a half-metallic ferrimagnet, as calculated using the generalized gradient exchange-correlation potential [86].

In addition to the mentioned study, other works (referenced as [35,86,87]) explored the exchange interactions in Ni_2MnZ ($Z = Ga, In, Sn, Sb$) and Mn_2VZ ($Z = Al, Ge$) alloys. Ni_2MnZ was found to be non-half-metallic, while Mn_2VZ was identified as half-metallic. These studies emphasized the significance of intersublattice exchange interactions. In the case of Mn_2VZ ($Z = Al, Ge$), it was observed that the ferrimagnetic coupling between V and Mn moments stabilized the ferromagnetic alignment of Mn moments. The V-based Heusler alloys Mn_2VZ ($Z = Al, Ga, In, Si, Ge, Sn$) were predicted to exhibit half-metallic ferrimagnetism in these studies [35,86,88].

Half-metallicity in the Mn_2VAl ferrimagnet was detected using resonant inelastic soft X-ray scattering (SX-RIXS) in the presence of a magnetic field [89]. When V L -edge excitation was applied, the findings revealed that the partial density of states for the V $3d$ states around the Fermi energy was minimal, and these states exhibited a relatively localized character. Conversely, when Mn L -edge excitation was used, the spectra were dominated by fluorescence and displayed clear magnetic circular dichroism, which showed significant dependence on the excitation photon energy. These experimental results were compared with theoretical predictions based on density-functional-theory band structure calculations, confirming the itinerant, spin-dependent nature of the Mn $3d$ states and the decay of the Mn $2p$ core states. This consistency in the experimental data aligns with the half-metallic behavior of the Mn $3d$ states.

The electronic structure and magnetic state of SGS materials are quite similar to HMF compounds in many ways. “Transition” from the HMF to the SGS state can occur during doping. Using the first-principles calculations within density functional theory, the authors of ref. [90] described such a transition by studying the magnetism and electronic structure of $\text{Co}_{2-x}\text{Mn}_{1+x}\text{Al}$ ($0 \leq x \leq 1$) alloys, i.e., during the transition from HMF Co_2MnAl to SGS Mn_2CoAl .

As reported in [90], the electronic spectrum of the Co_2MnAl compound ($x = 0$) exhibits an intersection of its spin-up and spin-down bands with the Fermi level E_F , indicating metallic properties for both spin directions. However, Co_2MnAl displays a low density of states for spin-down electrons, resulting in a pseudogap rather than a true gap. The calculated spectra show a spin polarization of approximately 75%. As the manganese content increases, the spin-down valence band of Co_2MnAl shifts downward, causing the density of states to approach zero. Consequently, the degree of spin polarization increases. In the case of the $\text{Co}_{1.5}\text{Mn}_{1.5}\text{Al}$ compound, as Mn content further increases, the top of the spin-down band aligns with the Fermi level, leading to the emergence of a genuine gap and achieving a maximum spin polarization of 100%. Despite that, $\text{Co}_{1.5}\text{Mn}_{1.5}\text{Al}$ faces a vulnerability as its Fermi level is situated at the edge of the spin-down bandgap, making it susceptible to external influences, especially structural defects.

As Mn content continues to rise in $\text{Co}_{2-x}\text{Mn}_{1+x}\text{Al}$, the spin-down valence band moves further away from the Fermi level, resulting in an enlarged band gap. At $x = 1.875$, the width of the spin-down gap reaches approximately 0.4 eV, with the Fermi level nearly positioned at the midpoint of the gap. This leads the authors of reference [90] to classify the $\text{Co}_{1.125}\text{Mn}_{1.875}\text{Al}$ compound as an “ideal” half-metallic ferromagnet. With increasing Mn content to $x = 2$, the compound transforms into an inverse Heusler alloy Mn_2CoAl . In this compound, a genuine energy gap is preserved for spin-down states. The electronic structure of Mn_2CoAl exhibits a unique characteristic: for spin-up electronic states, the conduction band and valence band edges

closely approach the Fermi level, resulting in a minimal energy gap. This distinctive feature categorizes the inverse Mn_2CoAl compound as a spin gapless semiconductor.

Table 1 presents information on Mn_2YZ and Mn_3Z ($Y = \text{Cr, Fe, Co}$; $Z = \text{Al, Ge, Si, Sn, Pt}$), for which the electronic state, magnetic state, and anomalous Hall conductivity are given.

Table 1. Manganese-based compounds of Mn_2YZ and Mn_3Z ($Y = \text{V, Cr, Fe, Co, Ni}$; $Z = \text{Al, Ge, Si, Sn, Pt, Ir}$). Electronic and magnetic states and anomalous Hall conductivity.

Compound	Electronic State	Magnetic State	Anomalous Hall Conductivity σ^{AHE} ($\text{Ohm cm})^{-1}$
Mn_2VAl	HMF ¹ [41]	FIM ² [41]	
Mn_2VSi	HMF [41]	FIM [41]	
Mn_2CrAl	HMF [91,92]	CFIM ³ [21]	
Mn_2FeAl	HMF [36]	CFIM [42] Frustrated AFM ⁴ [44]	
Mn_2NiAl		AFM [93]	
Mn_2CoAl	SGS ⁵ [47]	FM ⁶ [47]	21.8 [47]
Mn_3Al	HM-AFM ⁷ [94]	CFIM (cast); frustrated AFM (RMQ) ⁸ [28,29] AFM [94]	320 [62]
Mn_3Ge	HM-FIM ⁹ [94] TSM ¹⁰ [9]	FIM [94] Noncollinear AFM [9,63]	60 at RT; ~380 at 5 K [63]
Mn_3Si	HM-FIM [94]	FIM [94]	
Mn_3Sn	TSM [79]	Noncollinear AFM [78,81] kagome AFM [79]	~20 at RT; ~100 at 100 K [95]
Mn_3Pt	TSM [82]	kagome AFM [82]	100 [82]
Mn_3Ir		AFM [96]	40 at RT [96]

¹ HMF is a half metallic ferromagnet. ² FIM is a ferrimagnet. ³ CFIM is a compensated ferrimagnet. ⁴ AFM is an antiferromagnet. ⁵ SGS is a spin gapless semiconductor. ⁶ FM is a ferromagnet. ⁷ HM-AFM is a half-metallic antiferromagnet. ⁸ RMQ is rapid melt quenched. ⁹ HM-FIM is a half-metallic ferrimagnet. ¹⁰ TSM is a topological semimetal.

5. Conclusions

Intermetallic compounds based on manganese, specifically Mn_2YZ and Mn_3Z (where ($Y = \text{Sc, Ti, V, Cr, Fe, Co, etc.}$; $Z = \text{Al, Ge, Sn, Si, Pt, etc.}$), exhibit unique characteristics of the electronic structure. These compounds have the potential to exhibit various electronic and magnetic states, such as antiferromagnet, compensated ferrimagnet, topological semimetal, and frustrated antiferromagnet. Furthermore, their magnetic and electronic properties are highly sensitive to external influences.

In the electronic subsystem of Mn_2YAl compounds, different magnetic states can lead to the emergence of half-metallic ferromagnet and spin gapless semiconductor states. For instance,

Mn_2CoAl can exhibit a ferromagnetic spin gapless semiconductor state, while Mn_2FeAl can display a frustrated antiferromagnet state.

Compounds of Mn_3Z manifest as a half-metallic ferromagnet or a topological semimetal, displaying notable phenomena such as a large anomalous Hall effect, spin Hall effect, spin Nernst effect, and thermal Hall effect. The magnetic subsystem of these compounds can exhibit states such as ferrimagnetism, antiferromagnetism, compensated ferrimagnetism, frustrated antiferromagnetism, and antiferromagnetism with a kagome-type lattice. Overall, Mn_3Z compounds offer a rich spectrum of electronic and magnetic properties.

When comparing the properties of Mn compounds Mn_2YAl and Mn_3Z , it becomes evident that there are both similarities and differences between them, as shown in Table 1. In the electronic structure of Mn_2YAl alloys, the predominant state is that of a half-metallic ferromagnet, whereas in the Mn_2CoAl compound, it exhibits characteristics of a spin gapless semiconductor. It is worth noting that Mn_2CoAl is among the first Heusler alloys where the SGS state is prominently observed. In terms of magnetism, Mn_2YAl alloys display a range of behaviors, including ferromagnetism, compensated ferrimagnetism, and frustrated AFM state.

On the other hand, the Mn_3Z compounds exhibit more diverse electronic and magnetic states. Many of them demonstrate the characteristics of a topological semimetal with significant anomalous Hall conductivity, even at room temperature. Similar to Mn_2YAl alloys, they also exhibit a variety of magnetic states. Moreover, due to their richer electronic structure, they can realize states such as noncollinear AFM states and AFM states typical for a kagome-type lattice.

It should be emphasized that in actual materials, the presence and behavior of electronic and magnetic states, as well as transitions between them, can vary depending on various factors. These factors include the composition of the sample, external parameters such as temperature, magnetic field, and external pressure, as well as the dimensionality of the material (bulk, film, nanostructure), and the processing method used (cast, rapidly quenched, nanostructured samples, etc.). The electronic and magnetic states discussed, as well as the transitions between them, can be implemented and put into practice.

Besides the practical applications, all the states discussed, especially frustrated antiferromagnetism and half-metallic ferromagnetism, are of general scientific interest. Some systems considered can demonstrate anomalous electronic properties (particularly, large T -linear heat capacity) and are highly intriguing from a physical standpoint, posing an exciting challenge for future theoretical advancements.

It should be noted that a significant number of studies on manganese-based Heusler compounds exploit band calculations, which may not always be reliable. This is especially true when treating the size of the energy gap and the degree of spin polarization in the case of

possible HMF and SGS compounds, thereby overestimating the stability of these states. However, there are ongoing improvements in electronic structure calculation methods, and new modern techniques are emerging. It is essential to constantly compare these calculations with experimental data. For example, in the case of the HMF, this could involve comparing the results of band calculations and direct experiments to determine the gap and spin polarization in situ by ultraviolet-photoemission spectroscopy, taking advantage of a multichannel spin filter [97]. NMR experiments could also be conducted to search for the vanishing of a linear contribution to the temperature dependence of the nuclear spin-lattice relaxation rate $1/T_1$ (violation of Korringa's law), which is theoretically predicted for the HMF [34].

Finally, a promising direction for exploring new electronic effects and magnetic state features is a comprehensive study of quaternary Heusler alloys containing manganese atoms. Although the present review did not cover such compounds, there are many studies in this area, which can be found in related reviews [31,98,99] and references therein.

This opens up further opportunities for fine control of the magnetic and electronic characteristics of such compounds for their possible practical use in spintronics and micro- and nanoelectronics.

Author Contributions: Conceptualization, V.V.M. and V.Y.I.; methodology, V.V.M. and V.Y.I.; formal analysis, V.V.M. and V.Y.I.; investigation, V.V.M.; resources, V.V.M. and V.Y.I.; data curation, V.V.M. and V.Y.I.; writing—original draft preparation, V.V.M. and V.Y.I.; writing—review and editing, V.V.M. and V.Y.I.; visualization, V.V.M. and V.Y.I.; supervision, V.V.M. and V.Y.I.; funding acquisition, V.V.M. All authors have read and agreed to the published version of the manuscript.

Funding: The research was carried out within the state assignment of Ministry of Science and Higher Education of the Russian Federation (themes «Spin», № 122021000036-3 and «Quantum», № 122021000038-7). Section 3 “Features of the electronic transport and magnetic state of Mn_3Z ($Z = Al, Ge, Si, Sn, Pt$ etc.) compounds” was prepared with the financial support of the Russian Science Foundation within the framework of research project No. 22-22-00935.

Acknowledgments: The authors consider it their pleasant duty to thank their colleagues and co-authors Lukoyanov, A.V., Skryabin, Y.N., Marchenkova, E.B. for valuable discussions, and Perevozchikova, Y.A., Perevalova, A.N., Fominykh, B.M., Semiannikova, A.A., Emelyanova, S.M. for help with the design of the review.

Conflicts of Interest: The authors declare no conflict of interest.

References

1. Heusler, F. Über magnetische manganlegierungen. *Verh. Dtsch. Phys. Ges.* **1903**, *12*, 219.
2. Tavares, S.; Yang, K.; Meyers, M.A. Heusler alloys: Past, properties, new alloys, and prospects. *Prog. Mater. Sci.* **2023**, *132*, 101017. <https://doi.org/10.1016/j.pmatsci.2022.101017>.
3. Katsnelson, M.I.; Irkhin, V.Y.; Chioncel, L.; Lichtenstein, A.I.; De Groot, R.A. Half-metallic ferromagnets: From band structure to many-body effects. *Rev. Mod. Phys.* **2008**, *80*, 315–378. <https://doi.org/10.1103/RevModPhys.80.315>.
4. Marchenkov, V.V.; Irkhin, V.Y. Half-metallic ferromagnets, spin gapless semiconductors and topological semimetals based on Heusler alloys: Theory and experiment. *Phys. Metals Metallogr.* **2021**, *122*, 1133–1157. <https://doi.org/10.1134/S0031918X21120061>.
5. Galanakis, I. Slater–Pauling Behavior in Half-Metallic Heusler Compounds. *Nanomaterials* **2023**, *13*, 2010. <https://doi.org/10.3390/nano13132010>.
6. Wang, X.L. Proposal for a New Class of Materials: Spin Gapless Semiconductors. *Phys. Rev. Lett.* **2002**, *100*, 156404. <https://doi.org/10.1103/PhysRevLett.100.156404>.
7. Wang, X.; Li, T.; Cheng, Z.; Wang, X.-L.; Chen, H. Recent advances in Dirac spin-gapless semiconductors. *Appl. Phys. Rev.* **2018**, *5*, 041103. <https://doi.org/10.1063/1.5042604>.
8. Marchenkov, V.V.; Irkhin, V.Y.; Semiannikova, A.A. Unusual kinetic properties of usual Heusler alloys. *J. Supercond. Nov. Magn.* **2022**, *35*, 2153–2168. <https://doi.org/10.1007/s10948-022-06342-1>.
9. Manna, K.; Sun, Y.; Muechler, L.; Kübler, J.; Felser, C. Heusler, Weyl and Berry. *Nat. Rev. Mater.* **2018**, *3*, 244–256. <https://doi.org/10.1038/s41578-018-0036-5>.
10. Baidak, S.T.; Lukoyanov, A.V. Common topological features in band structure of RNiSb and RSb compounds for $R = \text{Tb, Dy, Ho}$. *Materials* **2023**, *16*, 242. <https://doi.org/10.3390/ma16010242>.
11. Bamgbose, M.K.; Ayedun, F.; Solola, G.T.; Musari, A.A.; Kenmoe, S.; Adebayo, G.A. Electronic, elastic, and thermoelectric properties of half-Heusler topological semi-metal HfIrAs from first-principles calculations. *Crystals* **2023**, *13*, 37. <https://doi.org/10.3390/cryst13010037>.
12. Khan, R.A.A.; Ghomashchi, R.; Xie, Z.; Chen, L. Ferromagnetic shape memory Heusler materials: Synthesis, microstructure characterization and magnetostructural properties. *Materials* **2018**, *11*, 988. <https://doi.org/10.3390/ma11060988>.
13. Pushin, V.; Korolyov, A.; Kuranova, N.; Marchenkova, E.; Ustyugov, Y. New metastable baroand deformation-induced phases in ferromagnetic shape memory Ni₂MnGa-based alloys. *Materials* **2022**, *15*, 2277. <https://doi.org/10.3390/ma15062277>.
14. Sokolovskiy, V.V.; Miroshkina, O.N.; Buchelnikov, V.D.; Marchenkov, V.V. Magnetocaloric effect in metals and alloys. *Phys. Metals Metallogr.* **2022**, *123*, 315. <https://doi.org/10.1134/S0031918X2204010X>.
15. dos Reis, R.D.; Caron, L.; Singh, S.; Felser, C.; Nicklas, M. Direct and indirect determination of the magnetocaloric effect in the Heusler compound Ni_{1.7}Pt_{0.3}MnGa. *Entropy* **2021**, *23*, 1273. <https://doi.org/10.3390/e23101273>.
16. Wollmann, L.; Nayak, A.K.; Parkin, S.S.P.; Felser, C. Heusler 4.0: Tunable Materials. *Annu. Rev. Mater. Res.* **2017**, *47*, 247. <https://doi.org/10.1146/annurev-matsci-070616-123928>.
17. Graf, T.; Felser, C.; Parkin, S.S.P. Simple rules for the understanding of Heusler compounds. *Prog. Solid State Chem.* **2011**, *39*, 1. <https://doi.org/10.1016/j.progsolidstchem.2011.02.001>.
18. Wollmann, L.; Chadov, S.; Kübler, J.; Felser, C. Magnetism in cubic manganese-rich Heusler compounds. *Phys. Rev. B* **2014**, *90*, 214420. <https://doi.org/10.1103/PhysRevB.90.214420>.
19. Zhang, Y.; Sun, Y.; Yang, H.; Železný, J.; Parkin, S.P.P.; Felser, C.; Yan, B. Strong anisotropic anomalous Hall effect and spin Hall effect in the chiral antiferromagnetic compounds Mn₃X ($X = \text{Ge, Sn, Ga, Ir, Ph, and Pt}$). *Phys. Rev. B* **2017**, *95*, 075128. <https://doi.org/10.1103/PhysRevB.95.075128>.
20. Jamer, M.E.; Wang, Y.J.; Stephen, G.M.; McDonald, I.; Grutter, A.J.; Sterbinsky, G.E.; Arena, D.A.; Borchers, J.A.; Kirby, B.J.; Lewis, L.H.; et al. Compensated ferrimagnetism in the zero-moment Heusler alloy Mn₃Al. *Phys. Rev. Appl.* **2017**, *7*, 064036. <https://doi.org/10.1103/PhysRevApplied.7.064036>.
21. Marchenkov, V.V.; Irkhin, V.Y.; Perevozchikova, Y.A.; Terent'ev, P.B.; Semiannikova, A.A.; Marchenkova, E.B.; Eisterer, M. Kinetic properties and half-metallic magnetism in Mn₂YAl Heusler alloys. *J. Exp. Theor. Phys.* **2019**, *128*, 919–925. <https://doi.org/10.1134/S1063776119060049>.
22. Yang, H.; Sun, Y.; Zhang, Y.; Shi, W.-J.; Parkin, S.S.P.; Yan, P. Topological Weyl semimetals in the chiral antiferromagnetic materials Mn₃Ge and Mn₃Sn. *New J. Phys.* **2017**, *19*, 015008. <https://doi.org/10.1088/1367-2630/aa5487>.

23. Ogasawara, T.; Kim, J.-Y.; Ando, Y.; Hirohata, A. Structural and antiferromagnetic characterization of noncollinear $D0_{19}$ Mn_3Ge polycrystalline film. *J. Magn. Magn. Mater.* **2019**, *473*, 7–11. <https://doi.org/10.1016/j.jmmm.2018.10.035>.
24. Tsidilkovski, I.M.; Harus, G.I.; Shelushinina, N.G. Impurity states and electron transport in gapless semiconductors. *Adv. Phys.* **1985**, *34*, 43–174. <https://doi.org/10.1080/00018738500101731>.
25. Liu, Z.H.; Tang, Z.J.; Tan, J.G.; Zhang, Y.J.; Wu, Z.G.; Wang, X.T.; Liu, G.D.; Ma, X.Q. Tailoring structural and magnetic properties of $Mn_{3-x}Fe_xGa$ alloys towards multifunctional applications. *IUCrJ* **2018**, *5*, 794–800. <https://doi.org/10.1107/s205225251801326x>.
26. Obambi, M.A.; Zagrebin, M.A.; Buchelnikov, V.D. Electronic Properties of Mn_3Z ($Z = Ga, Ge$) Alloys: Studies from First Principles. *Bull. Russ. Acad. Sci. Phys.* **2023**, *87*, 416–419. <https://doi.org/10.3103/s1062873822701362>.
27. Zhang, H.; Liu, W.; Lin, T.; Wang, W.; Liu, G. Phase Stability and Magnetic Properties of Mn_3Z ($Z = Al, Ga, In, Tl, Ge, Sn, Pb$) Heusler Alloys. *Appl. Sci.* **2019**, *9*, 964. <https://doi.org/10.3390/app9050964>.
28. Marchenkov, V.V.; Irkhin, V.Y.; Marchenkova, E.B.; Semiannikova, A.A.; Korenistov, P.S. Magnetic order and electronic transport properties in the Mn_3Al compound: The role of the structural state. *Phys. Lett. A* **2023**, *471*, 128803–128806. <https://doi.org/10.1016/j.physleta.2023.128803>.
29. Marchenkov, V.V.; Irkhin, V.Y.; Marchenkova, E.B.; Semiannikova, A.A.; Korenistov, P.S. The electrical resistivity, magnetic, and galvanomagnetic properties of a cast and rapid melt quenched Mn_3Al Heusler alloy. *Phys. Metals Metallogr.* **2023**, *124*, 321–327. <https://doi.org/10.1134/S0031918X23600318>.
30. Tas, M.; Şaşıoğlu, E.; Blügel, S.; Mertig, I.; Galanakis, I. Ab-initio calculation of the Hubbard U and Hund exchange J in local moment magnets: The case of Mn-based full Heusler compounds. *Phys. Rev. Mater.* **2022**, *6*, 114401. <https://doi.org/10.1103/physrevmaterials.6.114401>.
31. Elphick, K.; Frost, W.; Samiepour, M.; Kubota, T.; Takanashi, K.; Sukegawa, H.; Mitani, S.; Hirohata, A. Heusler alloys for spintronic devices: Review on recent development and future perspectives. *Sci. Technol. Adv. Mater.* **2021**, *22*, 235–271. <https://doi.org/10.1080/14686996.2020.1812364>.
32. Fan, L.; Chen, F.; Li, C.-m.; Hou, X.; Zhu, X.; Luo, J.-l.; Chen, Z.-Q. Promising spintronics: Mn-based Heusler alloys Mn_3Ga , Mn_2YGa ($Y=V, Nb, Ta$), $ScMnVGa$. *J. Magn. Magn. Mater.* **2020**, *497*, 166060. <https://doi.org/10.1016/j.jmmm.2019.166060>.
33. De Groot, R.A.; Mueller, F.M.; van Engen, P.G.; Buschow, K.H.J. New class of materials: Half-metallic ferromagnets. *Phys. Rev. Lett.* **1983**, *50*, 2024–2027. <https://doi.org/10.1103/PhysRevLett.50.2024>.
34. Irkhin, V.Y.; Katsnel'son, M.I. Half-metallic ferromagnets. *Physics-Uspekhi* **1994**, *37*, 659. <https://doi.org/10.1070/PU1994v037n07ABEH000033>.
35. Özdoğan, K.; Galanakis, I.; Şaşıoğlu, E.; Aktaş, B. Search for half-metallic ferrimagnetism in V-based Heusler alloys Mn_2VZ ($Z = Al, Ga, In, Si, Ge, Sn$). *J. Phys. Condens. Matter* **2006**, *18*, 2905. <https://doi.org/10.1088/0953-8984/18/10/013>.
36. Luo, H.Z.; Zhang, H.W.; Zhu, Z.Y.; Ma, L.; Xu, S.F.; Wu, G.H.; Zhu, X.X.; Jiang, C.B.; Xu, H.B. Half-metallic properties for the Mn_2FeZ ($Z = Al, Ga, Si, Ge, Sb$) Heusler alloys: A first-principles study. *J. Appl. Phys.* **2008**, *103*, 083908. <https://doi.org/10.1063/1.2903057>.
37. Luo, H.; Zhu, Z.; Liu, G.; Xu, S.; Wu, G.; Liu, H.; Qu, J.; Li, Y. Prediction of half-metallic properties for the Heusler alloys Mn_2CrZ ($Z = Al, Ga, Si, Ge, Sb$): A first-principles study. *J. Magn. Magn. Mater.* **2008**, *320*, 421–428. <https://doi.org/10.1016/j.jmmm.2007.06.021>.
38. Zenasni, H.; Faraoun, H.I.; Esling, C. First-principle prediction of half-metallic ferrimagnetism in Mn-based full-Heusler alloys with highly ordered structure. *J. Magn. Magn. Mater.* **2013**, *333*, 162–168. <https://doi.org/10.1016/j.jmmm.2013.01.003>.
39. Abbas Emami, S.A.; Amirabadizadeh, A.; Nourbakhsh, Z.; Baizae, S.M.; Alavi Sadr, S.M. Study of the structural, electronic, magnetic, and optical properties of Mn_2ZrGa full-Heusler alloy: First-principles calculations. *J. Supercond. Nov. Magn.* **2018**, *31*, 127–134. <https://doi.org/10.1007/s10948-017-4174-6>.
40. Abada, A.; Amara, K.; Hiadsi, S.; Amrani, B. First principles study of a new half-metallic ferrimagnets Mn_2 -based full Heusler compounds: Mn_2ZrSi and Mn_2ZrGe . *J. Magn. Magn. Mater.* **2015**, *388*, 59–67. <https://doi.org/10.1016/j.jmmm.2015.04.023>.
41. Buchelnikov, V.D.; Baigutlin, D.R.; Sokolovskiy, V.V.; Miroshkina, O.N. The influence of exchange correlation effects on the stabilization of the half-metallic properties of Mn_2VAl and Mn_2VSi alloys. *Phys. Metals Metallogr.* **2023**, *124*, 118–125. <https://doi.org/10.1134/S0031918X22601962>.

42. Gavrikov, I.; Seredina, M.; Zheleznyy, M.; Shchetinin, I.; Karpenkov, D.; Bogach, A.; Chatterjee, R.; Khovaylo, V. Magnetic and transport properties of Mn₂FeAl. *J. Magn. Magn. Mater.* **2019**, *478*, 55–58. <https://doi.org/10.1016/j.jmmm.2019.01.088>.
43. Mooij, J. Electrical conduction in concentrated disordered transition metal alloys. *Physica Status Solidi (a)* **1973**, *17*, 521–530. <https://doi.org/10.1002/pssa.2210170217>.
44. Dash, S.; Lukoyanov, A.V.; Nancy, Mishra, D.; Mohammed Rasi, U.P.; Gangineni, R.B.; Vasundhara, M.; Patra, A.K. Structural stability and magnetic properties of Mn₂FeAl alloy with a β-Mn structure. *J. Magn. Magn. Mater.* **2020**, *513*, 167205. <https://doi.org/10.1016/j.jmmm.2020.167205>.
45. Stinshoff, R.; Nayak, A.K.; Fecher, G.H.; Bake, B.; Ouardi, S.; Skourski, Y.; Nakamura, T.; Felser, C. Completely compensated ferrimagnetism and sublattice spin crossing in the half-metallic Heusler compound Mn_{1.5}FeV_{0.5}Al. *Phys. Rev. B* **2017**, *95*, 060410. <https://doi.org/10.1103/PhysRevB.95.060410>.
46. Ouardi, S.; Fecher, G.H.; Felser, C.; Kübler, J. Realization of spin gapless semiconductors: The Heusler compound Mn₂CoAl. *Phys. Rev. Lett.* **2013**, *110*, 100401. <https://doi.org/10.1103/PhysRevLett.110.100401>.
47. Ouardi, S.; Fecher, G.H.; Felser, C.; Kübler, J. Erratum: Realization of spin gapless semiconductors: The Heusler compound Mn₂CoAl. *Phys. Rev. Lett.* **2013**, *110*, 100401. *Phys. Rev. Lett.* **2019**, *122*, 059901. <https://doi.org/10.1103/PhysRevLett.122.059901>.
48. Feng, W.; Fu, X.; Wan, C.; Yuan, Z.; Han, X.; Quang, N.V.; Cho, S. Spin gapless semiconductor like Ti₂MnAl film as a new candidate for spintronics application. *Phys. Status Solidi RRL* **2015**, *9*, 641–645. <https://doi.org/10.1002/pssr.201510340>.
49. Shreder, E.I.; Makhnev, A.A.; Lukoyanov, A.V.; Marchenkov, V.V. Electron structure and optical properties of the Mn_{1.8}Co_{1.2}Al alloy and spin gapless semiconductor state. *Phys. Metals Metallogr.* **2018**, *119*, 1068–1072. <https://doi.org/10.1134/S0031918X18110194>.
50. Luo, P.; Wang, M.; Zheng, S.; Wang, Q.; Gan, L.-H.; Hui, Q. Tunable mechanical and half-metallic properties of Mn_{2-x}Fe_{1+x}Si alloys: A first principles investigation. *Phys. B Condens. Matter* **2021**, *615*, 413044. <https://doi.org/10.1016/j.physb.2021.413044>.
51. Životský, O.; Skotnicová, K.; Čegan, T.; Juřica, J.; Gembalová, L.; Zažímal, F.; Szurman, I. Structural and magnetic properties of inverse-Heusler Mn₂FeSi alloy powder prepared by ball milling. *Materials* **2022**, *15*, 697. <https://doi.org/10.3390/ma15030697>.
52. Sokolovskiy, V.; Zagrebin, M.; Baigutlin, D.; Buchelnikov, V. Ab initio prediction of coexistence of two magnetic states in Mn₂YSn (Y = Sc, Ti, and V) Heusler alloys under applied pressure. *Comput. Mater. Sci.* **2023**, *228*, 112365. <https://doi.org/10.1016/j.commatsci.2023.112365>.
53. Erager, K.R.; Baigutlin, D.R.; Sokolovskiy, V.V.; Buchelnikov, V.D. Exchange correlation effects in modulated martensitic structures of the Mn₂NiGa alloy. *Phys. Metals Metallogr.* **2022**, *123*, 375–380. <https://doi.org/10.1134/S0031918X22040044>.
54. Mityuk, V.I.; Rimskii, G.S.; Val'kov, V.I.; Golovchan, A.V.; Mashirov, A.V.; Koledov, V.V. Low temperature features of the magnetic and magnetocaloric properties of the Mn_{1-x}Co_xNiGe system (0.05 ≤ x ≤ 0.4). *Phys. Metals Metallogr.* **2022**, *123*, 386–391. <https://doi.org/10.1134/S0031918X22040081>.
55. Sokolovskiy, V.V.; Zagrebin, M.A.; Buchelnikov, V.D. Magnetocaloric effect in Mn₂YSn (Y = Sc, Ti, V) alloys. *Phys. Metals Metallogr.* **2023**, *124*, in press.
56. Kostenko, M.G.; Lukoyanov, A.V. Magnetic properties and electronic structure of Mn-Al alloys in the β-Mn structure. *J. Magn. Magn. Mater.* **2022**, *542*, 168600. <https://doi.org/10.1016/j.jmmm.2021.168600>.
57. Takatsu, H.; Yoshizawa, H.; Yonezawa, S.; Maeno, Y. Critical behavior of the metallic triangular-lattice Heisenberg antiferromagnet PdCrO₂. *Phys. Rev. B* **2009**, *79*, 104424. <https://doi.org/10.1103/PhysRevB.79.104424>.
58. Komleva, E.V.; Irkhin, V.Y.; Solovyev, I.V.; Katsnelson, M.I.; Streltsov, S.V. Unconventional magnetism and electronic state in the frustrated layered system PdCrO₂. *Phys. Rev. B* **2020**, *102*, 174438. <https://doi.org/10.1103/PhysRevB.102.174438>.
59. Wurmehl, S.; Kandpal, H.C.; Fecher, G.H.; Felser, C. Valence electron rules for prediction of half-metallic compensated-ferrimagnetic behaviour of Heusler compounds with complete spin polarization. *J. Phys. Condens. Matter* **2006**, *18*, 6171. <https://doi.org/10.1088/0953-8984/18/27/001>.
60. Knyazev, Y.V.; Lukoyanov, A.V.; Kuz'min, Y.I.; Dash, S.; Patra, A.K.; Vasundhara, M. Electronic structure and spectral characteristics of the Mn₃Al compound. *Phys. Metals Metallogr.* **2021**, *122*, 954–959. <https://doi.org/10.1134/S0031918X21100045>.
61. Vonsovskii, S.V. *Magnetism*; J. Wiley: New York, NY, USA, 1974.
62. Park, M.; Han, G.; Rhim, S.H. Anomalous Hall effect in a compensated ferrimagnet: Symmetry analysis for Mn₃Al. *Phys. Rev. Res.* **2022**, *4*, 013215. <https://doi.org/10.1103/PhysRevResearch.4.013215>.

63. Kiyohara, N.; Tomita, T.; Nakatsuji, S. Giant anomalous Hall effect in the chiral antiferromagnet Mn_3Ge . *Phys. Rev. Appl.* **2016**, *5*, 064009. <https://doi.org/10.1103/PhysRevApplied.5.064009>.
64. Jungwirth, T.; Marti, X.; Wadley, P.; Wunderlich, J. Antiferromagnetic spintronics. *Nat. Nanotechnol.* **2016**, *11*, 231–241. <https://doi.org/10.1038/nnano.2016.18>.
65. Baltz, V.; Manchon, A.; Tsoi, M.; Moriyama, T.; Ono, T.; Tserkovnyak, Y. Antiferromagnetic spintronics. *Rev. Mod. Phys.* **2018**, *90*, 015005. <https://doi.org/10.1103/RevModPhys.90.015005>.
66. Šmejkal, L.; Mokrousov, Y.; Yan, B.; MacDonald, A.H. Topological antiferromagnetic spintronics. *Nat. Phys.* **2018**, *14*, 242–251. <https://doi.org/10.1038/s41567-018-0064-5>.
67. Železný, J.; Wadley, P.; Olejník, K.; Hoffmann, A.; Ohno, H. Spin transport and spin torque in antiferromagnetic devices. *Nat. Phys.* **2018**, *14*, 220–228. <https://doi.org/10.1038/s41567-018-0062-7>.
68. Yan, H.; Feng, Z.; Qin, P.; Zhou, X.; Guo, H.; Wang, X.; Chen, H.; Zhang, X.; Wu, H.; Jiang, C.; et al. Electric-field-controlled antiferromagnetic spintronic devices. *Adv. Mater.* **2020**, *32*, 1905603. <https://doi.org/10.1002/adma.201905603>.
69. Chen, X.; Shi, S.; Shi, G.; Fan, X.; Song, C.; Zhou, X.; Bai, H.; Liao, L.; Zhou, Y.; Zang, H.; et al. Observation of the antiferromagnetic spin Hall effect. *Nat. Mater.* **2021**, *20*, 800–804. <https://doi.org/10.1038/s41563-021-00946-z>.
70. Kuroda, K.; Tomita, T.; Suzuki, M.T.; Bareille, C.; Nugroho, A.A.; Goswami, P.; Ochi, M.; Ikhlas, M.; Nakayama, M.; Akebi, S.; et al. Evidence for magnetic Weyl fermions in a correlated metal. *Nat. Mater.* **2017**, *16*, 1090–1095. <https://doi.org/10.1038/nmat4987>.
71. Li, X.; Xu, L.; Ding, L.; Wang, J.; Shen, M.; Lu, X.; Zhu, Z.; Behnia, K. Anomalous Nernst and Righi-Leduc effects in Mn_3Sn : Berry curvature and entropy flow. *Phys. Rev. Lett.* **2017**, *119*, 056601. <https://doi.org/10.1103/PhysRevLett.119.056601>.
72. Guo, G.-Y.; Wang, T.-C. Large anomalous Nernst and spin Nernst effects in the noncollinear antiferromagnets Mn_3X ($X = \text{Sn}, \text{Ge}, \text{Ga}$). *Phys. Rev. B* **2017**, *96*, 224415. <https://doi.org/10.1103/PhysRevB.96.224415>.
73. Chen, Y.; Gaudet, J.; Dasgupta, S.; Marcus, G.G.; Lin, J.; Chen, T.; Tomita, T.; Ikhlas, M.; Zhao, Y.; Chen, W.C.; et al. Antichiral spin order, its soft modes, and their hybridization with phonons in the topological semimetal Mn_3Ge . *Phys. Rev. B* **2020**, *102*, 054403. <https://doi.org/10.1103/PhysRevB.102.054403>.
74. Xu, L.; Li, X.; Lu, X.; Collignon, C.; Fu, H.; Koo, J.; Fauque, B.; Yan, B.; Zhu, Z.; Behnia, K. Finite-temperature violation of the anomalous transverse Wiedemann-Franz law. *Sci. Adv.* **2020**, *6*, eaaz3522. <https://doi.org/10.1126/sciadv.aaz3522>.
75. dos Reis, R.D.; Ghorbani Zavareh, M.; Ajeesh, M.O.; Kutelak, L.O.; Sukhanov, A.S.; Singh, S.; Noky, J.; Sun, Y.; Fischer, J.E.; Manna, K.; et al. Pressure tuning of the anomalous Hall effect in the chiral antiferromagnet Mn_3Ge . *Phys. Rev. Mater.* **2020**, *4*, 051401. <https://doi.org/10.1103/PhysRevMaterials.4.051401>.
76. Rai, V.; Stunault, A.; Schmidt, W.; Jana, S.; Perßon, J.; Soh, J.-R.; Brückel, T.; Nandi, S. Anomalous Hall effect and magnetic structure of the topological semimetal $(\text{Mn}_{0.78}\text{Fe}_{0.22})_3\text{Ge}$. *Phys. Rev. B* **2023**, *107*, 184413. <https://doi.org/10.1103/PhysRevB.107.184413>.
77. Takaesu, Y.; Uchima, K.; Nakamura, S.; Yogi, M.; Niki, H.; Hedo, M.; Nakama, T.; Tomiyoshi, S. Transport properties of Heusler compound Mn_3Si under high pressure. *J. Phys. Conf. Ser.* **2014**, *568*, 042033. <https://doi.org/10.1088/1742-6596/568/4/042033>.
78. Markou, A.; Taylor, J.M.; Kalache, A.; Werner, P.; Parkin, S.S.P.; Felser, C. Noncollinear antiferromagnetic Mn_3Sn films. *Phys. Rev. Mater.* **2018**, *2*, 051001. <https://doi.org/10.1103/PhysRevMaterials.2.051001>.
79. Li, X.; Koo, J.; Zhu, Z.; Behnia, K.; Yan, B. Field-linear anomalous Hall effect and Berry curvature induced by spin chirality in the kagome antiferromagnet Mn_3Sn . *Nat. Commun.* **2023**, *14*, 1642. <https://doi.org/10.1038/s41467-023-37076-w>.
80. Sharma, V.; Nepal, R.; Budhani, R.C. Planar Hall effect and anisotropic magnetoresistance in thin films of chiral antiferromagnet Mn_3Sn . *arXiv* **2023**, arXiv:2307.07795.
81. Zuniga-Cespedes, B.E.; Manna, K.; Noad, H.M.L.; Yang, P.-Y.; Nicklas, M.; Felser, C.; Mackenzie, A.P.; Hicks, C.W. Observation of an anomalous Hall effect in single-crystal Mn_3Pt . *New J. Phys.* **2023**, *25*, 023029. <https://doi.org/10.1088/1367-2630/acbc3f>.
82. Zhao, Z.; Zhang, K.; Guo, Q.; Jiang, Y. Strain-dependent magnetism and anomalous Hall effect in noncollinear antiferromagnetic Mn_3Pt films. *Phys. E Low-Dimens. Syst. Nanostructures* **2022**, *138*, 115141. <https://doi.org/10.1016/j.physe.2022.115141>.
83. De Groot, R.A.; Buschow, K.H.J. Recent developments in half-metallic magnetism. *J. Magn. Magn. Mater.* **1986**, *54–57*, 1377–1380. [https://doi.org/10.1016/0304-8853\(86\)90861-9](https://doi.org/10.1016/0304-8853(86)90861-9).

84. Kübler, J.; William, A.; Sommers, C. Formation and coupling of magnetic moments in Heusler alloys. *Phys. Rev. B* **1983**, *28*, 1745. <https://doi.org/10.1103/PhysRevB.28.1745>.
85. Ghosh, S.; Ghosh, S. Systematic understanding of half-metallicity of ternary compounds in Heusler and Inverse Heusler structures with 3d and 4d elements. *Phys. Scr.* **2019**, *94*, 125001. <https://doi.org/10.1088/1402-4896/ab0f6c>.
86. Weht, R.; Pickett, W.E. Half-metallic ferrimagnetism in Mn_2VAI . *Phys. Rev. B* **1999**, *60*, 13006–13010. <https://doi.org/10.1103/physrevb.60.13006>.
87. Şaşıoğlu, E.; Sandratskii, L.M.; Bruno, P. First-principles study of exchange interactions and Curie temperatures of half-metallic ferrimagnetic full Heusler alloys Mn_2VZ ($Z=Al, Ge$). *J. Phys. Condens. Matter* **2005**, *17*, 995. <https://doi.org/10.1088/0953-8984/17/6/017>.
88. Şaşıoğlu, E.; Sandratskii, L.M.; Bruno, P. First-principles calculation of the intersublattice exchange interactions and Curie temperatures of the full Heusler alloys Ni_2MnX ($X=Ga, In, Sn, Sb$) *Phys. Rev. B* **2004**, *70*, 024427. <https://doi.org/10.1103/physrevb.70.024427>.
89. Umetsu, R.Y.; Fujiwara, H.; Nagai, K.; Nakatani, Y.; Kawada, M.; Sekiyama, A.; Kuroda, F.; Fujii, H.; Oguchi, T.; Harada, Y.; et al. Half-metallicity of the ferrimagnet Mn_2VAI revealed by resonant inelastic soft x-ray scattering in a magnetic field. *Phys. Rev. B* **2019**, *99*, 134414. <https://doi.org/10.1103/physrevb.99.134414>.
90. Feng, Y.; Zhou, T.; Chen, X.; Yuan, H.; Chen, H. The effect of Mn content on magnetism and half-metallicity of off-stoichiometric Co_2MnAl . *J. Magn. Magn. Mater.* **2015**, *387*, 118–126. <https://doi.org/10.1016/j.jmmm.2015.04.002>.
91. Luo, H.; Zhu, Z.; Ma, L.; Xu, S.; Zhu, X.; Jiang, C.; Hu, H.; Wu, G. Effect of site preference of 3d atoms on the electronic structure and half-metallicity of Heusler alloy Mn_2YAl . *J. Phys. D Appl. Phys.* **2008**, *41*, 055010. <https://doi.org/10.1088/0022-3727/41/5/055010>.
92. Shreder, E.I.; Lukoyanov, A.V.; Makhnev, A.A.; Dash, S.; Patra, A.; Vasundhara, M. Electronic structure and optical properties of the Mn_2CrAl Heusler alloy. *Phys. Metals Metallogr.* **2020**, *121*, 532–536. <https://doi.org/10.1134/S0031918X20060125>.
93. Chernov, E.D.; Lukoyanov, A.V. Effect of electron correlations on the electronic structure and magnetic properties of the full Heusler alloy Mn_2NiAl . *Magnetochemistry* **2023**, *9*, 185. <https://doi.org/10.3390/magnetochemistry9070185>.
94. Gao, G.Y.; Yao, K.-L. Antiferromagnetic half-metals, gapless half-metals, and spin gapless semiconductors: The DO_3 -type Heusler alloys. *Appl. Phys. Lett.* **2013**, *103*, 232409. <https://doi.org/10.1063/1.4840318>.
95. Nakatsuji, S.; Kiyohara, N.; Higo, T. Large anomalous Hall effect in a non-collinear antiferromagnet at room temperature. *Nature* **2015**, *527*, 212–215. <https://doi.org/10.1038/nature15723>.
96. Iwaki, H.; Kimata, M.; Ikebuchi, T.; Kobayashi, Y.; Oda, K.; Shiota, Y.; Ono, T.; Moriyama, T. Large anomalous Hall effect in LI_2 -ordered antiferromagnetic Mn_3Ir thin films. *Appl. Phys. Lett.* **2020**, *116*, 022408. <https://doi.org/10.1063/1.5128241>.
97. Jourdan, M.; Minar, J.; Braun, J.; Kronenberg, A.; Chadov, S.; Balke, B.; Gloskovskii, A.; Kolbe, M.; Elmers, H.J.; Schoenhense, G.; et al. Direct observation of half-metallicity in the Heusler compound Co_2MnSi . *Nat. Commun.* **2014**, *5*, 3974. <https://doi.org/10.1038/ncomms4974>.
98. Gao, Q.; Opahle, I.; Zhang, H. High-throughput screening for spin-gapless semiconductors in quaternary Heusler compounds. *Phys. Rev. Mater.* **2019**, *3*, 024410. <https://doi.org/10.1103/PhysRevMaterials.3.024410>.
99. Seh, A.Q.; Gupta, D.C. Quaternary Heusler alloys a future perspective for revolutionizing conventional semiconductor technology. *J. Alloys Compd.* **2021**, *871*, 159560. <https://doi.org/10.1016/j.jallcom.2021.159560>.